Molecular Dynamics and Structural Studies of Zinc Chloroquine Complexes

Mirko Paulikat,[††] Daniele Vitone,[††] Florian K. Schackert,[††] Nils Schuth,[††] Alessandra Barbanente, GiovanniMaria Piccini, Emiliano Ippoliti, Giulia Rossetti, Adam H. Clark, Maarten Nachtegaal, Michael Haumann, Holger Dau, Paolo Carloni,* Silvano Geremia, Rita De Zorzi, Liliana Quintanar, and Fabio Arnesano

ABSTRACT: Chloroquine (CQ) is a first-choice drug against malaria and autoimmune diseases. It has been co-administered with zinc against SARS-CoV-2 and soon dismissed because of safety issues. The structural features of Zn−CQ complexes and the effect of CQ on zinc distribution in cells are poorly known. In this study, state-of-the-art computations combined with experiments were leveraged to solve the structural determinants of zinc−CQ interactions in solution and the solid state. NMR, ESI-MS, and X-ray absorption and diffraction methods were combined with *ab initio* molecular dynamics calculations to address the kinetic lability of this complex. Within the physiological pH range, CQ binds Zn^{2+} through the quinoline ring nitrogen, forming $[Zn(CQH)Cl_x(H_2O)_{3-x}]^{(3+)-x}$ ($x = 0$, 1, 2, and 3) tetrahedral complexes.

The $Zn(CQH)Cl_3$ species is stable at neutral pH and at high chloride concentrations typical of the extracellular medium, but metal coordination is lost at a moderately low pH as in the lysosomal lumen. The pentacoordinate complex $[Zn(CQH)(H_2O)_4]^{3+}$ may exist in the absence of chloride. This *in vitro*/*in silico* approach can be extended to other metal-targeting drugs and bioinorganic systems.
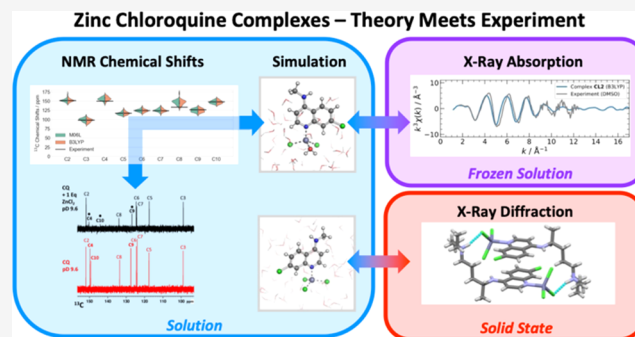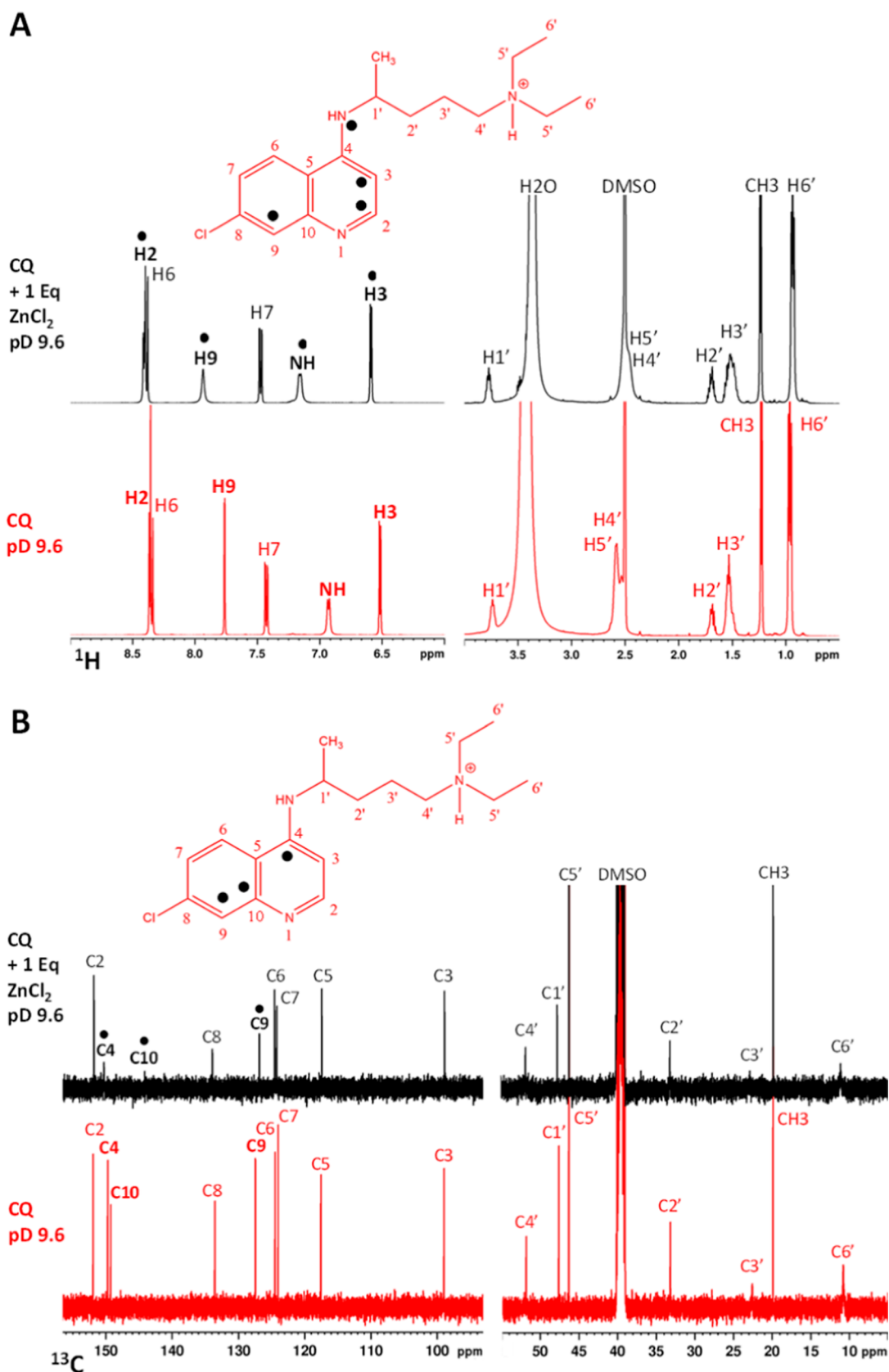
INTRODUCTION

Chloroquine (CQ) is a first-choice drug against malaria,[1] which accumulates in the digestive vacuole of the *Plasmodium* parasite. The latter invades the red blood cells, causing the digestion of the host hemoglobin and release of iron-containing heme molecules.[2] Since free heme is toxic to *Plasmodium*, it must be packed into hemozoin crystals for the parasite to survive.[2] X-ray microscopy indicates that CQ (along with other quinoline antimalarial drugs) can cap hemozoin crystals, thus inhibiting their growth.[3] In the parasite digestive vacuole, the pH value is in the range of 4.5–4.9.[4] At this acidic pH, CQ reaches a submillimolar concentration, that is, about 1000-fold more than that of the drug in the culture medium.[3] The 4-aminoquinoline moiety is protonated (doubly positively charged) and undergoes trapping in these lysosome-related organelles.[5,6] The lysosomal targeting (lysosomotropism) of CQ may be responsible for its antimalarial properties,[7] and endosomal alkalinization can lead to inhibition of infections.[8]

CQ is also used as a drug against autoimmune diseases, such as lupus erythematosus and rheumatoid arthritis.[1] In addition, the accumulation of CQ in acidic organelles can lead to the dysfunction of several enzymes required for proteolytic processing and post-translational modification of viral proteins.[9]

Recently, CQ has been used for the emergency treatment of SARS-CoV-2 infection, either alone or in combination with zinc ions.[10−12] The latter exhibit antiviral properties[13] and activate immune cells.[14] However, the mechanism of action of Zn−CQ complexes is unclear, and the risk/benefit ratio of CQ proved too high to consider this drug as safe and effective.[15] It has also been proposed that CQ acts as a Zn^{2+} ionophore, that is, a molecule capable of promoting the cellular uptake of zinc ions.[16] Yet, recent evidence indicates that hydroxychloroquine, a closely related drug, does not carry Zn^{2+} across the biological membranes,[17] making the role of CQ as a zinc ionophore highly controversial.

Figure 1. (A) 1D ^{1}H and (B) 1D ^{13}C NMR spectra of free CQ (red) and CQ with 1 equiv of $ZnCl_2$ (black) in DMSO-d_6 (pD 9.6). The structure of CQ with atom numbering is shown at the top of each panel. The ^{1}H and ^{13}C signals experiencing significant shifts upon Zn^{2+} binding are marked with black dots. The assignment is reported on top of each peak. The signals of residual H_2O and DMSO-d_5 are also indicated.

The structural determinants of Zn−CQ complexes, together with the impact of CQ on the intracellular distribution of zinc, remain largely unknown. A complex scenario is expected. Zinc complexes (d^{10} electronic configuration) are highly labile and variable in their coordination because of the lack of ligand field stabilization. This allows for the dynamic coordination environments of zinc ions that adopt different coordination numbers (from four to six) in interactions with substrates. Zinc ions in an aqueous solution are known to be hexa-coordinated, exchanging water molecules with a rate of ~0.05 ns^{-1}.[18] In proteins, zinc ions are commonly tetrahedrally coordinated by O-, N-, or S-atoms from glutamate/aspartate/water, histidine, or cysteine residues. Instead, chlorido ligands can replace water molecules in zinc−aquo complexes to form a series of hexa- and tetra-coordinated species of formula $[ZnCl_x(H_2O)_{6-x}]^{(2+)-x}$ (x = 0, 1) and $[ZnCl_x(H_2O)_{4-x}]^{(2+)-x}$ (x = 2, 3, and 4), respectively, depending on specific conditions, such as chloride concentrations and pH values.

In the presence of CQ, the acid−base properties, tautomerism, and conformational flexibility of the ligand can strongly influence the coordination stereochemistry of the metal ion. Navarro et al.[19,20] have indicated that CQ and its diphosphate form (CQDP) can bind Zn^{2+} through different N donor atoms. The authors reported the synthesis of Zn−CQ complexes starting from chloride and acetate Zn^{2+} salts; in particular, for the former salt, they indicated the formation of a pentacoordinate $[ZnCl_2(CQ)(H_2O)_2]$ complex on the basis of the CHN elemental analysis, but no structure is available in the Cambridge Structural Database.

To go beyond the limitations of a single structural characterization technique, we investigated the coordination chemistry of Zn−CQ complexes by leveraging data from different experimental techniques, each giving valuable insights into the complex behavior of an apparently simple system (i.e., ESI-MS in the gas phase, nuclear magnetic resonance (NMR) in solution, X-ray diffraction in the crystalline state, and X-ray absorption in the frozen and crystalline states). These different techniques are complemented by non-empirical molecular dynamics simulations. Our combined in vitro/in silico approach allows us to elucidate the structural features and speciation of Zn−CQ complexes, which would certainly play a determining role in how CQ impacts metal ion distribution within the cell.

RESULTS AND DISCUSSION

Experimental Studies on Zn−CQ Complexes. *Nuclear Magnetic Resonance and MS.* CQ was obtained from commercial racemic CQDP by chemical extraction.[21] NMR analysis confirmed the removal of the phosphate groups: the 1D ^{31}P NMR spectrum of free CQ in DMSO-d_6 shows the absence of any phosphorus signal, and the 2D $^1H−^{13}C$ HSQC spectrum shows that protons H5′ and H4′ are shifted upfield compared to the spectrum of CQDP (Figure S1A−C). Removal of phosphate groups is important as their presence impacts the coordination of Zn^{2+} ions (Figure S1D). A pD-dependent titration allowed us to determine the pK_a values of the quinoline nitrogen (pK_{a1} = 7.3 ± 0.2) and the tertiary aliphatic nitrogen (pK_{a2} = 9.5 ± 0.1) by monitoring the chemical shift (CS) changes of the neighboring ^1H nuclei in the 1D NMR spectra (Figure S2). Moreover, by changing the pD values from 13.4 to 3.8, a remarkable downfield shift of the proton bound to the secondary aliphatic nitrogen was observed, with an inflection point of the interpolating curve at a pD value close to pK_{a1}. This shift is due to the protonation

of the quinoline nitrogen, which influences the amino/imino tautomerism of the secondary aliphatic nitrogen.[22] The acquisition of 2D $^1H−^{13}C$ HMBC NMR spectra at different pD values allowed us to observe a deshielding of the C4 signal (from 149.7 to 155.5 ppm) at lower pD values, confirming the conversion of the secondary aliphatic nitrogen to the imino form (Figure S3).

Based on the measured pK_a values, CQ is predicted to concentrate more in lysosomes/vacuoles (pH ~4.6) than in the extracellular fluid (pH ~7.4), as recently reported in the case of basic local anesthetics,[23] because the doubly charged species has a more favorable hydration free energy than the singly protonated and neutral ones. However, additional CQ concentrating mechanisms (e.g., binding to heme) may be operative.[24]

In order to obtain information on Zn^{2+} coordination, the NMR spectra of free CQ in DMSO-d_6 and of an equimolar CQ/$ZnCl_2$ solution were collected at a pD of 9.6 (~pK_{a2}). Based on the pK_a values, this condition corresponds to a partial protonated state of tertiary amine and a full deprotonated state of quinoline. The 1D ^1H NMR spectrum of CQ with 1 equiv of $ZnCl_2$ displayed a deshielding of H9, H3, and NH signals (Figure 1A), while the 1D ^{13}C NMR spectrum showed a decrease in intensity and an upfield shift of C9 and C10 (Figure 1B), supporting Zn^{2+} coordination to the quinoline nitrogen. A complete ^{13}C resonance assignment of CQ in the absence and presence of $ZnCl_2$ was performed by analyzing the 2D $^1H−^{13}C$ HSQC and HMBC spectra (Figure S4). 1D ^1H NMR spectra were also recorded at lower pD values (7.9 and 5.9). While at pD 7.9, a behavior similar to that of CQ at pD 9.6 was observed, that is, deshielding of H9, H3, and NH signals upon Zn^{2+} addition; at an acidic pH, no variation of CSs was detected, consistent with having a protonated quinoline nitrogen that is not available to coordinate Zn^{2+} (Figure S5). Based on the pK_{a1} value, we estimated a 300-fold increase in the apparent dissociation constant of the Zn−CQ complex on passing from pH 7.4, as present in the extracellular fluid, to pH 4.6 in lysosomes/vacuoles.

The ESI-MS spectrum (recorded in the positive-ion mode) of CQ with 1 equiv of $ZnCl_2$ in DMSO-d_6 displays a main signal at m/z 494.0294 that can be assigned to $[C_{18}H_{27}Cl_4N_3Zn + H]^+$ singly charged species, corresponding to a Zn^{2+} ion coordinated to a CQ molecule and three chlorido ligands. The formation of this complex is also supported by the calculated isotope mass distribution, which closely matches the experimental set of peaks (Figure S6).

Paramagnetic Co^{2+} has been used as a probe to confirm the preferred Zn^{2+} anchoring site based on the similar coordination properties of the two metal ions.[25,26] NMR monitoring was conducted by performing a titration of free CQ with up to 1 equiv of $CoCl_2$ in DMSO-d_6. The Co^{2+} ion (d^7, high spin) caused paramagnetic shifts and broadening of signals around the coordination site; substoichiometric additions of $CoCl_2$ mostly affected H2, H3, and H9 protons adjacent to the quinoline nitrogen, which experienced the largest line broadening in the 1D ^1H NMR spectra (Figure S7A). Consistently, the signals of C2, C3, C9, and quaternary carbons C5 and C10 broadened in the 1D ^{13}C spectra (Figure S7B). In contrast, the ^1H and ^{13}C signals of the aliphatic chain were not affected until the end of the titration, confirming that metal coordination only occurs at the CQ aromatic nitrogen. This Zn−CQ interaction contrasts with that observed for the heme−CQ complexes that are relevant in the antimalarial activity of CQ.

As mentioned above, CQ can cap hemozoin crystals, inhibiting the *Plasmodium* parasite's growth.[3] Spectroscopic and molecular dynamics (MD) studies suggest that the two molecules interact non-covalently through π-stacking and cation−π interactions, with a nearly co-planar arrangement of the quinoline and porphyrin rings.[27] Axial coordination of the drug to heme iron appears less likely, considering that nitrogen donor atoms are protonated at the acidic pH of parasitic digestive vacuoles.

X-ray Crystallography. Small single crystals of the Zn−CQ complex were analyzed by X-ray diffraction at 100 K using synchrotron radiation. The asymmetric unit of the orthorhombic crystals contains one zwitterionic tri-chloro−chloroquinium−zinc complex, $Zn(CQH)Cl_3$ (Figure 2). One ethyl
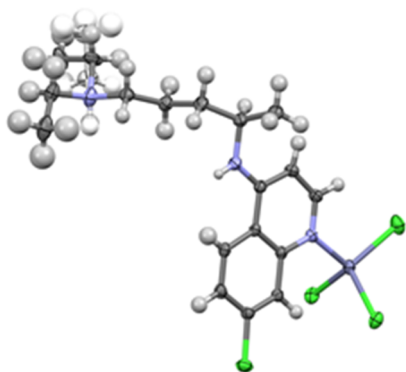

Figure 2. Asymmetric unit of the $Zn(CQH)Cl_3$ complex, with an anisotropic ellipsoid representation of non-H atoms. Ellipsoids are shown at the 50% probability level. The atom species are in CPK colors with alternative positions of the disordered ethyl groups in paler colors.

group shows a two-position disorder with 0.5 occupancy factors. The *Pbca* centrosymmetric space group implies that these crystals are composed by a racemic mixture of the enantiomeric complexes.

The Zn^{2+} ions are coordinated with a distorted tetrahedral geometry (Table S2) by three chloride ions and by the quinoline N-atom of a chloroquinium (CQH^+) ligand (Figure 2). The Zn−N distance of 2.051(1) Å is significantly shorter than that found in the tri-chloro−quinoline−zinc complex by about 0.04 Å.[28] The Zn−Cl bond lengths range from 2.2308(8) to 2.3086(6) Å, with the shortest distance in agreement with the mean value of the Zn−Cl bond lengths in the tri-chloro−Zn^{2+} complexes coordinated to $N(sp^2)$ ligands [2.239(3) Å].[29] The chloride ion coordinated with the longer Zn−Cl bond length forms an intermolecular H-bond. In fact, the crystal packing of the $Zn(CQH)Cl_3$ complex (Figure S9) shows the assembly of centrosymmetric dimeric species (Figure 3). The dimer is stabilized by two equivalent intermolecular H-bonds involving this coordinated chloride ion and the protonated tertiary ammine [a Cl···N distance of 3.152(2) Å] and by stacking interactions between the aromatic quinoline moieties (interplanar distance of 3.38 Å) as evidenced by the Hirshfeld surface mapped with the normalized contact distance (Figure S10). We conclude that the rather distorted tetrahedral geometry of the complex may arise from its dimerization and from relevant intermolecular contacts present in the solid state.

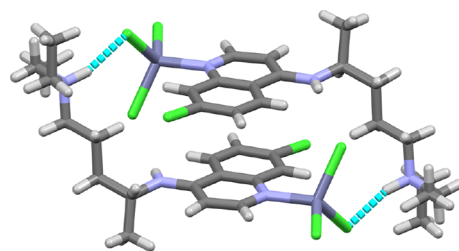*X-ray Absorption Spectroscopy of the Zn−CQ Complexes.* X-ray absorption spectroscopy (XAS) was used to probe the

Figure 3. Stick representation of dimeric assembly of the $Zn(CQH)$-Cl_3 complex. The atomic species are in CPK colors. For the sake of clarity, only one position of the disordered ethyl group is shown. H-bonds are evidenced with cyan dashed lines. The dimers are located on crystallographic inversion centers.

coordination properties of zinc bound to CQ. The Zn−CQ complexes in a frozen solution in DMSO (with 10% residual H_2O) and in crystallized form were studied by Zn K-edge XAS to elucidate and compare the coordination sphere around the metal ion in both solution and the solid state. The maximum intensity and the overall similarity of the normalized X-ray absorption near-edge structure (XANES) spectra (Figure 4A) indicate a nearly tetrahedral geometry in both complexes. Extended X-ray absorption fine structure (EXAFS) analysis (Figure 4B and Table S3) of both complexes converge to a four-coordinated zinc. In the case of crystallized Zn−CQ, in agreement with XRD analysis, zinc coordination features three chlorido ligands and one nitrogen atom. Coordination to the quinoline N-atom of CQ is supported by the secondary sphere with three carbon atoms corresponding to the quinoline atoms C2, C9, and C10 (see scheme in Figure 1). For Zn−CQ frozen in DMSO, a decrease of the extended EXAFS envelope at $k > 6$ $Å^{-1}$ is observed, as compared to the crystallized Zn−CQ, clearly indicating that fewer heavy atoms were bound to zinc. Indeed, EXAFS analysis reveals that the Zn−CQ complex in solution displays a metal coordination sphere with one nitrogen atom, only two chloride ions, and an oxygen-based ligand. A similar coordination sphere was observed for the powder Zn−CQ complex synthesized from DMSO, except for the presence of two more chloride ions at a distance above 3.3 Å, probably due to the packing effects (Figure S11 and Table S3). Overall, these results indicate that the zinc coordination sphere in the Zn−CQ complex in solution is quite similar to that of crystallized Zn−CQ, except that the oxygen ligand in the former is replaced by a chloride ion in the crystal, supporting the notion that three chlorido ligands are favored by crystallization conditions.

Molecular Dynamics of Zn−CQ Complexes in an Aqueous Solution. Our experimental investigations reveal important characteristics of zinc chloride reacting with CQ in different protonation states (CQ, CQH^+, and CQH_2^{2+}), in anhydrous conditions and in the presence of DMSO and/or water. Specifically, NMR measurements identify the binding site of a Zn^{2+} ion to the quinolinic nitrogen atom of CQ in a DMSO/water solution at room temperature. X-ray crystallography studies showed that, under anhydrous conditions in the solid state, (i) the zinc binds to the quinolinic nitrogen atom also here and (ii) three chlorido ligands and CQ form a distorted tetrahedral complex. EXAFS measurements support the notion of a tetrahedral geometry for the Zn−CQ complex, both in the frozen DMSO solution and in the solid state. EXAFS analysis also shows that the Zn^{2+} coordination sphere changes from having three chlorides in the crystal form to two
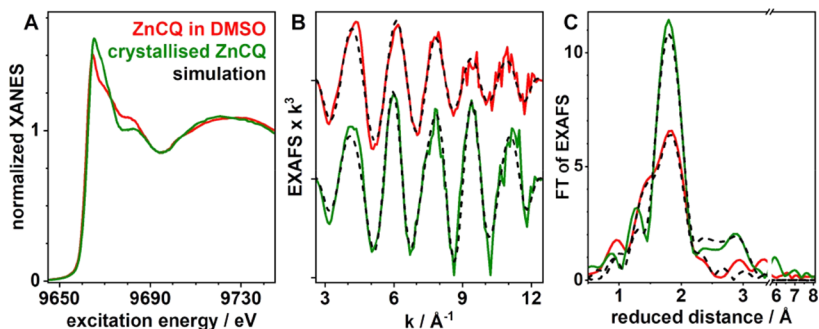
Figure 4. Zn K-edge XAS of Zn−CQ frozen in DMSO-d_6 (red) and in crystallized form (green) reveals a four-coordinated Zn with two chlorido ligands in DMSO and three chlorides in the crystal form. Shown are normalized XANES (A), extended EXAFS (B), and Fourier transform of EXAFS (C). Black dashed lines in (B,C) correspond to the fits of EXAFS spectra using simulation parameters given in Table S3.

chlorides in the frozen DMSO solution. Finally, the ESI-MS spectra reveal the formation of a tetra-coordinate complex [Zn(CQH$_2$)Cl$_3$]$^+$ in the gas phase. Taken together, these experiments suggest that the Zn^{2+} ion in the water solution binds to one CQ molecule in its quinolinic nitrogen, with chlorido ligands and water molecules completing a tetrahedral coordination. A penta-coordinated chloro complex, such as that originally proposed by Navarro et al.[19] ([ZnCl$_2$(CQ)(H$_2$O)$_2$]), might also exist in the aqueous solution.

Here, the structural dynamics of the latter, along the tetra- and penta-coordinated complexes in Figures 5 (left) and 6, are
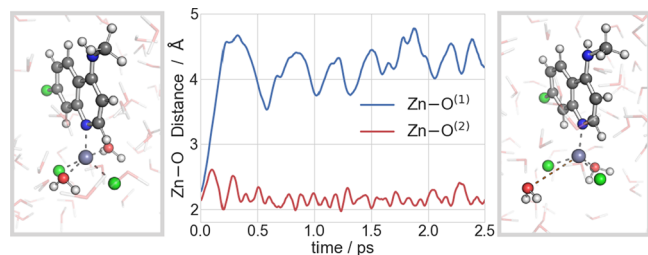

Figure 5. A water molecule dissociates from the [Zn(CQ$_m$)Cl$_2$(H$_2$O)$_2$] complex (left) to form [Zn(CQ$_m$)Cl$_2$(H$_2$O)] (**CL2**, right) in the AIMD. The plot in the middle reports the distances between the two water ligands and the zinc ion as a function of simulation time. One of them dissociates from the zinc ion already after 0.5 ps of AIMD.

investigated by *ab initio* molecular dynamics (AIMD) simulations at room temperature using the BLYP and B3LYP exchange−correlation functionals.[30] The complexes are immersed by around 110 water molecules, and the entire system is treated from first principles. Thus, in our simulation

setup, the ligands may enter or abandon the Zn^{2+} coordination sphere during the dynamics.

Approximately 15 ps of simulations for each complex was used for analysis and for comparison with the NMR and EXAFS data measured in this work. Additionally, approximately 5 ps simulations were collected for specific complexes at the more accurate (and far more expensive) B3LYP level of theory. We use a truncated model of the CQ molecule (indicated as CQ$_m$) in which the aliphatic chain is replaced by a methyl group for computational convenience. This replacement is expected not to affect the Zn^{2+} coordination chemistry. This is supported by NMR measurements with Co^{2+} that do not show the formation of chelates (Figure S7).

Our AIMD simulations suggest that the proposed chloro−aquo complex [Zn(CQ$_m$)Cl$_2$(H$_2$O)$_2$] from the work of Navarro et al.[19] is not stable in water (Figure 5). It loses a water ligand readily in the sub-ps timescale to yield [Zn(CQ$_m$)Cl$_2$(H$_2$O)] (**CL2**). This finding is corroborated by quantum chemical calculations, which favors unambiguously the tetra-coordination over a penta-coordination in an implicit solvent at the DLPNO-CCSD(T1)/def2-(S/TZ)VP// B3LYP/def2-TZVP[31−36] level of theory (Section S5 in the Supporting Information).[37] We next discuss the simulations of the complexes in Figure 6, all of them featuring the Zn−CQ moiety with water and/or chlorido ligands.

CL2 features two coordinating chloride ions and one water molecule to complete a distorted tetrahedral coordination of the metal ion. The electrostatic repulsion of the chloride ions causes a significantly larger Cl$^{(1)}$−Zn−Cl$^{(2)}$ angle of 114 ± 6°, as compared to the O−Zn−Cl$^{(1)}$ and O−Zn−Cl$^{(2)}$ angles of 103 ± 6° and 105 ± 7°, respectively. The calculated coordination bond distances of the Zn−N^{CQ}, Zn−O$^{(1)}$, Zn−Cl$^{(1)}$, and Zn−Cl$^{(2)}$ bonds are 2.07 ± 0.07, 2.10 ± 0.08, 2.35 ±

CL2 − [Zn(CQ$_m$)Cl$_2$(H$_2$O)]   **CL3** − [Zn(CQ$_m$)Cl$_3$]$^-$ **CL** − [Zn(CQ$_m$)Cl(H$_2$O)$_2$]$^+$ **WAT3** − [Zn(CQ$_m$)(H$_2$O)$_3$]$^{2+}$ **WAT4** − [Zn(CQ$_m$)(H$_2$O)$_4$]$^{2+}$
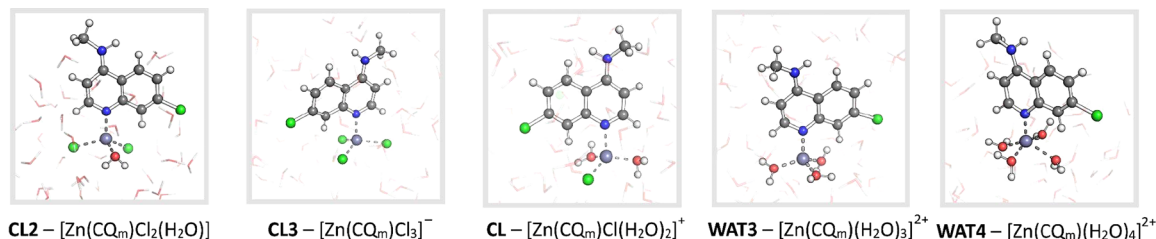
Figure 6. Overview of Zn−CQ$_m$ complexes with varying numbers of chloride and water ligands from AIMD simulations in an aqueous solution. The atomic species are colored in slate blue (Zn), green (Cl), red (O), white (H), gray (C), and blue (N). The overall potential energies of the complexes are reported in Table S6. For **CL2**, we include a picture of the electrostatic potential mapped onto its electron density isosurface in the Supporting Information (Figure S13).

0.09, and 2.29 ± 0.06 Å, respectively (see the Supporting Information for details). The chloride ions form hydrogen bonds to the water that would weaken the metal−ligand bond and would cause an increase in bond lengths. Indeed, given the relatively large atomic size of chloride, the Cl−Zn bonds are ∼0.2 Å longer than the water− and CQ_m−Zn bonds. The Zn-donor atom bond lengths are likely to be overestimated by BLYP-based calculations.[38,39] Indeed, they turn out to be shortened by up to 0.05 Å when using the more accurate B3LYP functional (Table S4).

Next, we turn our attention to the electronic properties: (i) the Mulliken charge of the Zn^{2+} ion is +0.85 ± 0.03 e, suggesting that the charge transfer from the ligands increases the electronic charge density at the Zn^{2+} ion. This effect has already been observed for Zn complexes and Zn^{2+} ions bound to proteins by pioneering studies of Merz and co-workers.[40−42] In fact, fluctuating Zn^{2+} charges comprise a major challenge for the simulation of Zn^{2+} complexes,[40−42] which is fully addressed here by AIMD. Such an effect has also been seen in other cases where divalent metal ions were involved in catalysis.[43,44] (ii) The Wannier centers (WCs) along the chemical bonds can be used to describe their polarity.[45] The WCs along the $Zn−N^{CQ}$, $Zn−Cl^{(1/2)}$, and $Zn−O^{(1)}$ bonds are located at the donor atoms with a fractional distance (defined as the difference between the Zn−WC and ligand atom−WC distances, which are normalized to the corresponding bond length) of ∼0.75, ∼0.75, and ∼0.83 from the metal ion, respectively. These results indicate a slightly stronger polarization of the CQ_m and chlorido ligands compared to the water molecule, consistent with the well-known Hard-Soft Acid-Base concept.[46]

CL3 results from the replacement of a Zn-bound water molecule in **CL2** with chloride. The simulation reveals a stable, almost regular, tetra-coordinated complex with averaged Zn−Cl distances in the range of 2.35−2.37 Å and Cl−Zn−Cl angles between 107 and 109°, reflecting the equivalence of the chlorido ligands in solution. The hydrogen bonds weaken the coordination bonds as discussed, causing an increase in bond lengths (see also Figure S9 and Table S2 in the Supporting Information). The average $Zn−N^{CQ}$ bond distance of 2.07 ± 0.06 Å is similar to that observed for **CL2** (Table S4).[47]

The Mulliken charge of the Zn^{2+} ion (+0.78 ± 0.03 e) is lower than that of **CL2**, possibly because the chlorido ligands are more polarizable than water. The fractional distances of WCs are comparable to those of $Zn−N^{CQ}$ and Zn−Cl bonds (∼0.75).

We finally analyze two tetrahedral complexes, featuring a number of chloride and water molecules not emerging from experiments: (i) in **CL** (Figure 6), a chloride in **CL2** is replaced by a water molecule. **CL** retains a distorted tetrahedral coordination, with the $Cl^{(1)}−Zn−O^{(1/2)}$ angles (both 110 ± 7°) larger than the $O^{(1)}−Zn−O^{(2)}$ angle (102 ± 7°). The $Zn−N^{CQ}$ and $Zn−Cl^{(1)}$ bond lengths are shortened by ∼0.05 Å relative to **CL2** and **CL3** (see the Supporting Information for details), possibly because the effective charge of the zinc ion (+0.94 ± 0.03 e) increases on passing from **CL** to **CL2/3**. In turn, this might be caused by the fact that the water ligand is less polarizable than chloride. The Zn−O bond lengths are also slightly shortened relatively to the one in **CL2** for increased charge on the metal ion (Table S4). (ii) In **WAT3**, no chloride ligand is present. The Zn^{2+} effective charge further increases (+1.03 ± 0.04 e), while the $Zn−N^{CQ}$ and Zn−O bond lengths decrease by ∼0.2−0.3 Å relative to **CL** (Table S4). Remarkably, in a simulation replica with different

initial positions and velocities than the first one, a fourth water molecule binds to the metal ion to form the penta-coordinated complex **WAT4**. Its geometry is in between a square-pyramidal and trigonal-bipyramidal structure. The average $Zn−N^{CQ}$ distance is found to be 2.06 ± 0.06 Å, slightly larger than that in **WAT3** (2.02 ± 0.06 Å). The Zn−O distances of **WAT4** are longer than those of **WAT3** and also show larger fluctuations. AIMD simulations on **WAT4** using the more accurate (and expensive) B3LYP functional show that the coordination bond lengths are, as expected, shortened, while the Zn−O bond lengths still fluctuate, but less so (Table S4). We conclude that both Zn−CQ−aquo complexes (**WAT3** and **WAT4**) may be present as intermediate species in aqueous solutions and demonstrate the flexibility of zinc coordination chemistry, as previously observed. Indeed, theoretical studies predicted the presence of two different coordinations on Zn^{2+}−diamine−aquo complexes,[48] and transient conversion of tetra- and penta-coordination may play a role for the zinc-dependent alcohol dehydrogenase function.[49,50]

Comparison with NMR Data. In the pool of experimental data reported here, the NMR experiments in solution reflect the most similar conditions to the water solution environment simulated by the theoretical calculations. The difference in the solvent conditions between the experiment (90% DMSO/10% water) and theory (water) is expected to have a minor effect on the CSs because both solvents are highly polar. There are no hydrogen bond acceptors in the complexed CQ ligand, besides the chlorine atom bonded to the C8 atom of CQ.[51] Figure 7 (and Figures S14 and S15) shows the distributions of the ^1H and ^{13}C CSs calculated using M06L[52] and B3LYP[34,35] functionals. The latter have been shown to predict accurately CSs.[53]
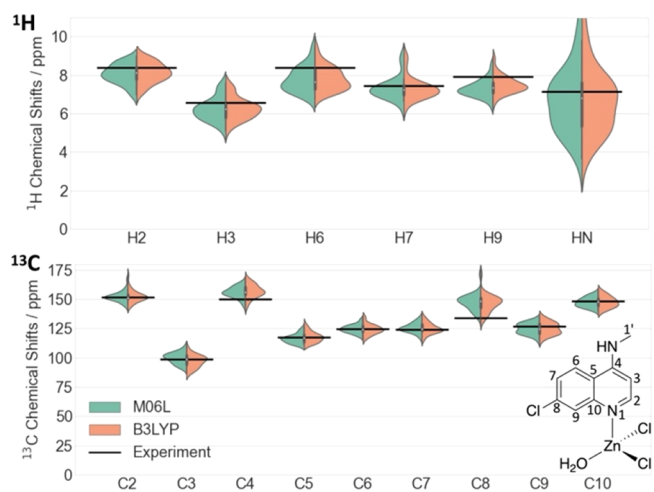

Figure 7. Calculated ^1H and ^{13}C NMR CS distributions using DFT with M06L[52] and B3LYP[34,35] functionals for complex **CL2** compared with the experimental data (black lines). Insets: structural formula of complex **CL2** indicating the atom numbering.

Our predictions are consistent with the experiments. The distributions of the calculated signals are much broader than the experimental ones.[54]

^1H Spectra. H2 and H6 nuclei (Figure 7) are the most deshielded nuclei, experimentally observed at 8.41 and 8.39 ppm, respectively. The calculated CSs cover this spectral region, with fluctuations between 7.5 and 8.5 ppm. In contrast, the H3 nucleus is predicted to resonate around 6 ppm,

consistent with the experimentally measured value of 6.59 ppm. Also, the predictions of H7 and H9 are consistent with the experimental spectrum. The calculated HN CSs show a very broad distribution. This is not surprising since it involves hydrogen bonds to solvent molecules that sensitively modulate the electronic density at the HN nucleus.

¹³C Spectra. The nuclei C2, C4, and C10 are predicted to resonate around 150 ppm in excellent agreement with experiment (151.8, 150.2, and 148.4 ppm, respectively). These nuclei are directly bonded to nitrogen atoms, either to the quinolinic nitrogen or the exocyclic amine group, causing the downfield shift. The calculations also reproduce the experimentally observed aromatic signal at 98.9 ppm for the C3 nucleus. In between, we identified, consistently with the experiment, the C5, C6, C7, and C9 nuclei of the CQ ligand. The largest discrepancy is observed for the CS distribution of the C8 nucleus. The calculated shifts fluctuate around ~150 ppm, while the experimental signal peaks at lower fields of 133.7 ppm. This carbon atom is bonded to a chlorine that can act as a hydrogen bond acceptor in water solution. In turn, water can polarize the chlorine atom, making it a stronger electron-withdrawing substituent. As a result, the C8 signal is shifted downfield in comparison to the experimental signal in DMSO.

Comparison with EXAFS Data. The conditions in our simulations (water at 300 K) differ significantly from the experimental one (frozen solution of DMSO with 10% residual H_2O at 20 K). The k^3-weighted spectrum and Fourier transform of **CL2** best reproduces the experimental spectrum for the Zn−CQ complex (Figures 8 and S16). The calculations
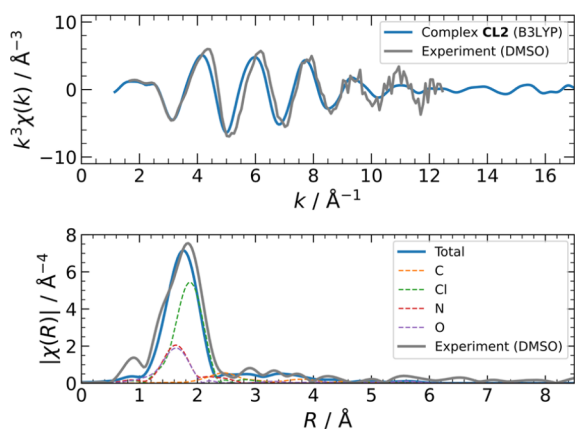

Figure 8. k^3-Weighted EXAFS spectrum (top) and Fourier transform (bottom) calculated from the AIMD-B3LYP simulation of **CL2** in comparison to the experimental spectrum.

are carried out at the B3LYP level of theory. In spite of the different conditions, the averaged Zn−N^{CQ} bond distances agree well with the experiment (Tables S3 and S4). The Zn−O and Zn−Cl distances in the calculated structures are larger than those derived from the EXAFS fit by ~0.08−0.1 Å, possibly due to the hydrogen bonding interactions with the solvent that weakens the metal−ligand bonds, as discussed previously. On the other hand, the Fourier transform of the spectrum differs slightly. In particular, a shoulder at low effective distances (~1.5 Å), which arises from the N^{CQ} and O donor atoms (see the discussion above), is resolved only in the experimental spectrum. The difference can be explained by the

temperature effects that cause larger fluctuations in the bond distances at room-temperature conditions.

Comparison with the X-ray Data. The calculated bond lengths of Zn−N^{CQ} and one of the Zn−Cl bonds of **CL3** compare fairly well with those in the X-ray structure (Tables S2 and S4). The other two Zn−Cl bonds are far shorter in the X-ray structure because, unlike the first, they are not involved in the H-bonding interactions (Figure 3). The calculated, tetrahedral geometry of the complex differs markedly from that in the X-ray structure, which is distorted because of the packing forces present only in the crystal.

In conclusion, our simulations reproduce fairly well the observed experimental spectral properties of the Zn−CQ complexes, within the limitations associated with the limited timescale investigated. The calculations allow us to suggest a tetra-coordination in solution when chloride is bound (complexes **CL**, **CL2**, and **CL3**) or a mixture of a tetra- and penta-coordination when only water is present (complexes **WAT3** and **WAT4**).

CONCLUSIONS

The interaction of the zinc ion with low-molecular-weight ligands, such as water, inorganic anions, and organic molecules, is highly relevant in biology, but, contrary to its coordination in proteins, it has been poorly discussed in the biochemical literature.[55] Most of the studies rely on crystal structures, which allow only a few snapshots of the system but may not reproduce the complex behavior/dynamics in the solution revealed by modern molecular spectroscopy methods.

Here, we studied the effect of adding $ZnCl_2$ to purified CQ. The Zn^{2+} complex was characterized by a combination of state-of-the-art molecular simulations along with solution NMR, ESI-MS, and X-ray absorption and diffraction methods. The CQ coordination turns out to be strictly related to its acid−base properties and to the protonation state of nitrogen atoms, which in turn are linked to the ability of CQ to cross biological membranes and accumulate into acidic organelles. In the physiological pH range, CQ binds to Zn^{2+} through the quinoline ring nitrogen in a tetrahedral complex with three chloride ions or two chloride ions and a water molecule completing the coordination sphere to yield a zwitterionic or cationic complex, respectively (Chart 1). The former is stable at neutral pH and at high chloride concentrations typical of the extracellular medium; however, metal coordination is lost at

Chart 1
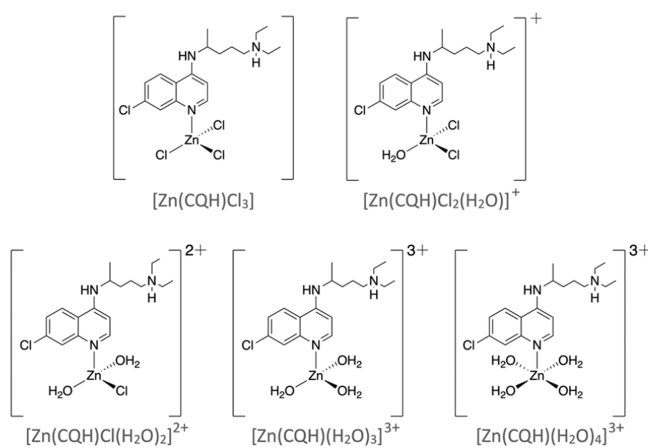
moderately low pH as in the lysosomal lumen. In light of the recent data on hydroxychloroquine,[17] monodentate quinoline ligands without auxiliary groups are unlikely to act as Zn^{2+} ionophores.

The two characterized complexes can be derived from the reaction of CQ with the two most abundant species present in a $ZnCl_2$ solution, namely, $[ZnCl_3(H_2O)]^-$ and $[ZnCl_2(H_2O)_2]$,[56] by substitution of a water molecule. AIMD simulations of these complexes are fully consistent with the experimental data and further suggest the existence of aqueous species with higher water content (Chart 1). Among the complexes in Chart 1, $[Zn(CQH)Cl_2(H_2O)]^+$ is not only fully consistent with NMR, but it is also the complex that best reproduces the EXAFS spectral data.

Overall, our combined *in vitro/in silico* approach has elucidated the structural determinants of Zn–CQ complexes, and it can be applied to other metal-targeting drugs and bioinorganic systems.

■ EXPERIMENTAL AND COMPUTATIONAL SECTION

NMR. CQ has been obtained from commercial CQDP by chemical extraction, following a procedure reported in the literature.[21] Elemental analysis and NMR were performed to check the purity of the extracted ligand. The calculated values for $C_{18}H_{26}N_3Cl \cdot 2H_3PO_4 \cdot 2H_2O \cdot 2CH_3OH$ (CQDP) are as follows: C, 38.99%; H, 7.19%; and N, 6.82%. The found values are as follows: C, 39.43%; H, 8.25%; and N, 7.39%. For purified CQ, the calculated values for $C_{18}H_{26}N_3Cl$ are as follows: C, 67.58%; H, 8.19%; and N, 13.13%. Found: C, 67.34%; H, 7–05%; N, 13.03%. The Zn–CQ complex was prepared in solution by adding 1 equiv of $ZnCl_2$ in 500 μL of CQ DMSO-d_6 solution (4.5 mM or 9 mM).

NMR samples were prepared by dissolving CQ with and without 1 equiv of $ZnCl_2$ in DMSO-d_6 at a concentration of 4.5 mM or 9 mM, and the pD value was adjusted with $DClO_4$ or NaOD using the relationship pD = pH* + 0.4 (where pH* is a direct reading in the D_2O solution of the H_2O-calibrated pH-meter). 1D ^1H and 2D ^1H–^{13}C HSQC and HMBC NMR spectra were recorded at 298.15 K on a Bruker Avance 300 Ultrashield spectrometer equipped with a double-resonance broad-band probe with Z-Gradient. 1D ^1H NMR spectra were acquired with a relaxation delay of 1.5 s, 64 scans, 32K data points, and a spectral width of 21 ppm. 2D ^1H–^{13}C HSQC and HMBC spectra were acquired with a recycle delay of 1.5 s. Each time domain was the average of 64 scans consisting of 1K complex data points over an F2 (^1H) spectral width of 13.35 ppm; the second dimension was derived from 256 increments with an F1 (^{13}C) spectral width of 250 ppm centered at 75 ppm. For HSQC spectra, an INEPT delay $1/(4 \cdot {}^1J_{C-H})$ of 1.72 ms ($^1J_{C-H}$ = 145 Hz) was used, and decoupling during acquisition was achieved using the standard GARP scheme. 1D ^{13}C NMR spectra were acquired on an Agilent 500/54 Premium Shielded spectrometer and with power-gated decoupling using a 20° flip angle and a relaxation delay of 2.0 s. Each spectrum consisted of 16K scans, 32K data points, and a spectral width of 300 ppm (^{13}C carrier at 130 ppm). All data were processed with Bruker software Topspin (version 3.5). Before Fourier transformation, an exponential multiplication with a line broadening (LB) of 0.30 and 2 Hz was applied for 1D ^1H and 1D ^{13}C spectra, respectively. 2D spectral data, zero-filled in F1 to 1K data points, were subjected to apodization using a squared cosine bell function in both dimensions prior to Fourier transformation and phase

correction. ^1H and ^{13}C CSs were referenced to residual DMSO-d_5 (δ^1H = 2.50 ppm and $\delta^{13}C$ = 39.52 ppm).

NMR-monitored pD titration experiments were used to determine site-specific pK_a values of CQ. The ligand was dissolved in 500 μL of DMSO-d_6 and transferred to an NMR tube. The pD of the sample was adjusted to the required value by adding $DClO_4$ or NaOD solutions and measured using a 3 mm diameter electrode for NMR tubes. The pD–titration curves were fitted using the following equation through GraphPad Prism 7.0 software

$$\delta_{obs} = \delta_p + \frac{\Delta\delta}{1 + 10^{(pK_a - pD)}} \quad (1)$$

where δ_{obs} is the CS observed at each pD value, δ_p is the CS of the fully protonated species, and $\Delta\delta$ is the CS variation between the end and the beginning of the titration.[57]

X-ray Crystallography. Single crystals suitable for X-ray investigation were obtained by slow cooling and evaporation of a methanol solution of racemic CQ and zinc chloride in a 1:1.4 molar ratio (detailed description of the synthesis in the Supporting Information). Large rectangular transparent crystals were obtained after 1 day (Figure S8).

Data collection was carried out at the XRD1 beamline of the Elettra synchrotron (Trieste, Italy), employing the rotating crystal method with a Dectris Pilatus 2M area detector. The crystal was cryoprotected with Parabar 10312 and kept under a nitrogen stream at a 100 K during data collection. The structure was solved using direct methods and refined by full-matrix least-squares (FMLS) methods on F^2, with anisotropic thermal parameters for all non-hydrogen atoms. Crystallographic data and refinement details are reported in Table S1 and in the Supporting Information.

X-ray Absorption Spectroscopy. XAS at the Zn K-edge was performed at beamline KMC-3 at BESSY-II (Berlin, Germany) using the previously described setup: storage ring operated in the top-up mode at 300 mA, a double-crystal Si[111] monochromator with a bandwidth of ~2 eV, a 13-element energy-resolving silicon drift detector (RaySpec) for fluorescence monitoring, and a sample held in a cryostat (Oxford) at 20 K.[58] The X-ray spot size on the sample was set by a focusing mirror and slits to about 4.0 mm × 1.5 mm. XAS at the Zn K-edge was also performed at the synchrotron SLS (Villigen, Switzerland) at the SuperXAS superbending magnet beamline with the storage ring operated in the top-up mode (400 mA) using a setup for XAS as previously described.[59] Signal-to-noise ratios were improved by averaging up to four spectra collected on different sample spots to avoid any unlikely photodamage for Zn^{2+} complexes. XAS spectra were averaged after detector dead-time and self-absorption correction, normalized to derive XANES spectra, and extended EXAFS spectra were extracted as described earlier.[60] The monochromator energy axis was calibrated (accuracy ±0.1 eV) using the first inflection point at 9659 eV in the simultaneously measured absorption spectrum of a Zn foil as a standard. Averaging, normalization, and extraction of EXAFS oscillations and conversion of the energy scale to the wave vector (k) scale were performed as previously described.[58] The k^3-weighted EXAFS spectra were simulated ($S0^2$ = 1.00) by a least-squares procedure using phase functions calculated with FEFF8-lite[61] and Fourier transforms (FTs) were calculated using the in-house software SimX using k-range of 1.7–12.4 Å^{-1} and cos windows extending over 10% at both k-range ends.[62,63] SimX uses the Levenberg–Marquardt (damped least-squares)

algorithm. The E0 used for the extraction of EXAFS oscillations was 9659 eV, and the E0 was refined to about (9654 ± 1) eV in the EXAFS fitting.

AIMD in Explicit Water. The first system simulated here is the $[Zn(CQ)Cl_2(H_2O)_2]$ complex, with the chloride and water ligands in the *trans* position. The aliphatic side chain at the CQ exocyclic nitrogen was replaced by a methyl group to reduce the system size without significantly affecting the interactions of the zinc ion binding to the quinolinic nitrogen (model "CQ_m"). The complex was pre-optimized at B3LYP/def2-SVP in the gas phase[34−36] and then solvated in a pre-equilibrated water box of $15.0 \times 16.8 \times 15.7$ Å using the GROMACS solvate tool.[64] The resulting system consisted of 112 water molecules and 361 atoms in total. This corresponds to a bulk water density of 0.89 g·mL^{-1}, commonly observed in AIMD simulations.[65,66] The quantum problem was solved using plane wave-based DFT.[67] We employed the BLYP functional with a plane wave cutoff of 100 Ry and norm-conserving Troullier−Martins pseudopotentials.[68] The system was initially optimized for 1100 steps. AIMD simulations within the Born−Oppenheimer scheme were carried out in the *NVT* ensemble. A time step of 0.48 fs was used. The system was first heated up with a rate of 0.024 K fs^{-1} to 300 K in 0.96 ps using the Berendsen thermostat with a coupling constant of 5000 a.u.,[69] followed by additional 0.96 ps for relaxation of the solvent at 300 K. In this preparation process, the coordinates of the complex were constrained. Then, the system was free to evolve for 19.2 ps at 300 K. The temperature was kept constant using a Nosé−Hoover thermostat, with a frequency of 5000 cm^{-1}.[70,71] The system quickly lost a water molecule to form **CL2** (Figure 5). The last 14.4 ps were used for analyses of **CL2**. The other tetra complexes in Figure 6 were built from **CL2** by replacing a chloride with a water molecule or the other way around. They then followed the same computational protocol, undergoing 19.2 ps AIMD simulations at 300 K. **CL2** and **WAT4** (Figure 6) underwent 5.28 ps AIMD with the B3LYP exchange−correlation functional, starting from the final AIMD snapshots using BLYP. The same setting as mentioned above was used, except that here we used a multiple time step framework for which high-level forces were evaluated at B3LYP and intermediate steps at BLYP.[72] Benchmark calculations revealed a time step factor of 5 as a reasonable choice (Figure S12). The last 4.80 ps were collected for analysis. AIMD-BLYP simulations of CQ_m in water were also run. The initial structure was obtained by replacing the zinc and chloride ions with water molecules in **CL2**. It underwent 19.2 ps of AIMD-BLYP at 300 K using the same computational protocol as mentioned above. The duration of 14.8 ps was collected for analysis. The calculations were carried out with CPMD 4.3.[73] The following properties were calculated: (i) geometrical quantities (and WCs[45]), calculated every 4.8 fs (0.24 ps) of AIMD-BLYP, and (ii) ^{1}H and ^{13}C NMR CSs and the Mulliken charges were calculated every 0.48 ps of AIMD-BLYP using ORCA 5.0.1.[53,74] The CSs were calculated as the mean traces of chemical shielding tensors of systems containing the Zn^{2+} ions, the CQ_m ligand, the chloride ions, and water molecules with a 5 Å distance around the Zn−CQ_m moiety (149−185 atoms). The tensors were obtained using the coupled perturbed self-consistent field approach, using the gauge-including atomic orbitals, as implemented, and benchmarked for the ORCA program.[53,74] The M06L[52] and B3LYP[34,35] functionals, along with the pc-sSeg-2 basis set, were used.[75] Two-electron Coulomb integrals were approxi-

mated with the resolution-of-the-identity method using the auxiliary def2-TZVP/JK basis set,[76,77] while the chain-of-sphere algorithm was employed for the two-electron exchange terms.[78] ORCA's very tight convergence settings and large grid specification were used.[74] Polarization from the bulk water phase was included by the conductor-like polarizable continuum model using a dielectric constant of 80.4.[79] The calculated CSs were then shifted to an appropriate reference value by averaging the calculated CSs of H7/C7 nuclei in CQ_m and setting to zero the difference between those and the correspondent experimental values. We then subtracted all the calculated CSs by the quantities required to set these differences to zero. (iii) EXAFS spectra at the zinc edge, calculated every 0.048 ps from AIMD-BLYP and AIMD-B3LYP using FEFF6L.[80−82] The zinc ion, the water molecules within 7.5 Å from it, the CQ_m ligand, and the chloride ions were included in the calculations (136−207 atoms). A real phase space shift of 5 eV was used. The real space representation was then determined by Fourier transformation of the k^3-weighted EXAFS spectra using the Larch module implemented in Python.[83] For this purpose, the spectral data in the k-vector interval of 2.5−12.5 Å^{-1} and the Kaiser−Bessel window function was applied. Atom-type-specific contributions were identified through their backscattering contributions. All properties were obtained as averages, except for the CSs, which are presented as distributions in Figure 7.

DATA AND SOFTWARE AVAILABILITY

NMR data were processed with the Bruker software Topspin 3.5 (https://www.bruker.com). Isotopic distributions for the ESI-MS experiments were calculated with the program Molecular Weight Calculator (https://omics.pnl.gov/software/molecular-weightcalculator). For single-crystal X-ray diffraction, data were indexed and integrated using the XDS package, while scaling was carried out with XSCALE (https://xds.mr.mpg.de/). The structure was solved using the SHELXT program, and refinement was performed with SHELXL-18/3 operating through the WinGX GUI (http://www.chem.gla.ac.uk/~louis/software/wingx/). XAS data were analyzed with the Feff8-lite program (https://feff.phys.washington.edu/feffproject-feff.html), and Fourier transforms were calculated with an in-house software. *Ab initio* molecular dynamics were carried out using CPMD 4.3 (http://www.cpmd.org). Configurationally averaged EXAFS spectra were calculated using the Feff6L program (https://feff.phys.washington.edu/feffproject-feff.html). All quantum chemistry calculations were carried out with the ORCA 5.0.1 program package (https://www.orcasoftware.de/). Graphical representations and structural formula were created with the licensed PyMOL 2.5.2 (https://pymol.org/2/) and ChemDraw Professional 21.0.0.28 programs (https://perkinelmerinformatics.com/), respectively.

◼ AUTHOR INFORMATION

Corresponding Author

Paolo Carloni − *Computational Biomedicine (IAS-5/INM-9), Forschungszentrum Jülich GmbH, 52428 Jülich, Germany; Department of Physics, RWTH Aachen University, 52062 Aachen, Germany;* ◉ orcid.org/0000-0002-9010-0149; Email: p.carloni@fz-juelich.de

Authors

Mirko Paulikat − *Computational Biomedicine (IAS-5/INM-9), Forschungszentrum Jülich GmbH, 52428 Jülich, Germany;* ◉ orcid.org/0000-0001-8403-2138

Daniele Vitone − *Department of Chemistry, University of Bari "Aldo Moro", 70125 Bari, Italy*

Florian K. Schackert − *Computational Biomedicine (IAS-5/INM-9), Forschungszentrum Jülich GmbH, 52428 Jülich, Germany; Department of Physics, RWTH Aachen University, 52062 Aachen, Germany;* ◉ orcid.org/0000-0001-6028-3717

Nils Schuth − *Department of Chemistry, Center for Research and Advanced Studies (Cinvestav), 07360 Mexico City, Mexico*

Alessandra Barbanente − *Department of Chemistry, University of Bari "Aldo Moro", 70125 Bari, Italy*

GiovanniMaria Piccini − *Euler Institute, Università Della Svizzera Italiana, 6962 Lugano, Switzerland*

Emiliano Ippoliti − *Computational Biomedicine (IAS-5/INM-9), Forschungszentrum Jülich GmbH, 52428 Jülich, Germany;* ◉ orcid.org/0000-0001-5513-8056

Giulia Rossetti − *Computational Biomedicine (IAS-5/INM-9), Forschungszentrum Jülich GmbH, 52428 Jülich, Germany; Jülich Supercomputing Centre (JSC), Forschungszentrum Jülich GmbH, 52428 Jülich, Germany; Department of Neurology, RWTH Aachen University, 52062 Aachen, Germany;* ◉ orcid.org/0000-0002-2032-4630

Adam H. Clark − *Paul Scherrer Institute, 5232 Villigen, Switzerland;* ◉ orcid.org/0000-0002-5478-9639

Maarten Nachtegaal − *Paul Scherrer Institute, 5232 Villigen, Switzerland;* ◉ orcid.org/0000-0003-1895-9626

Michael Haumann − *Department of Physics, Freie Universität Berlin, 14195 Berlin, Germany*

Holger Dau − *Department of Physics, Freie Universität Berlin, 14195 Berlin, Germany;* ◉ orcid.org/0000-0001-6482-7494

Silvano Geremia − *Department of Chemical and Pharmaceutical Sciences, University of Trieste, 34127 Trieste, Italy;* ◉ orcid.org/0000-0002-0711-5113

Rita De Zorzi − *Department of Chemical and Pharmaceutical Sciences, University of Trieste, 34127 Trieste, Italy*

Liliana Quintanar − *Department of Chemistry, Center for Research and Advanced Studies (Cinvestav), 07360 Mexico City, Mexico;* ◉ orcid.org/0000-0003-3090-7175

Fabio Arnesano − *Department of Chemistry, University of Bari "Aldo Moro", 70125 Bari, Italy;* ◉ orcid.org/0000-0002-8399-0964

Complete contact information is available at:
https://pubs.acs.org/10.1021/acs.jcim.2c01164

◼ REFERENCES

(1) Rynes, R. I. Antimalarial Drugs in the Treatment of Rheumatological Diseases. *Rheumatology* **1997**, *36*, 799−805.

(2) Weissbuch, I.; Leiserowitz, L. Interplay Between Malaria, Crystalline Hemozoin Formation, and Antimalarial Drug Action and Design. *Chem. Rev.* **2008**, *108*, 4899−4914.

(3) Kapishnikov, S.; Staalsø, T.; Yang, Y.; Lee, J.; Pérez-Berná, A. J.; Pereiro, E.; Yang, Y.; Werner, S.; Guttmann, P.; Leiserowitz, L.; Als-Nielsen, J. Mode of Action of Quinoline Antimalarial Drugs in Red Blood Cells Infected by Plasmodium Falciparum Revealed in Vivo. *Proc. Natl. Acad. Sci.* **2019**, *116*, 22946−22952.

(4) Hayward, R.; Saliba, K. J.; Kirk, K. The PH of the Digestive Vacuole of Plasmodium Falciparum Is Not Associated with Chloroquine Resistance. *J. Cell Sci.* **2006**, *119*, 1016−1025.

(5) Homewood, C. A.; Warhurst, D. C.; Peters, W.; Baggaley, V. C. Lysosomes, PH and the Anti-Malarial Action of Chloroquine. *Nature* **1972**, *235*, 50−52.

(6) Krogstad, D. J.; Schlesinger, P. H. A Perspective on Antimalarial Action: Effects of Weak Bases on Plasmodium Falciparum. *Biochem. Pharmacol.* **1986**, *35*, 547−552.

(7) Schultz, K. R.; Gilman, A. L. The Lysosomotropic Amines, Chloroquine and Hydroxychloroquine: A Potentially Novel Therapy for Graft-Versus-Host Disease. *Leuk. Lymphoma* **1997**, *24*, 201−210.

(8) Al-Bari, Md. A. A. Targeting Endosomal Acidification by Chloroquine Analogs as a Promising Strategy for the Treatment of Emerging Viral Diseases. *Pharmacol. Res. Perspect.* **2017**, *5*, No. e00293.

(9) Savarino, A.; Boelaert, J. R.; Cassone, A.; Majori, G.; Cauda, R. Effects of chloroquine on viral infections: an old drug against today's diseases. *Lancet Infect. Dis.* **2003**, *3*, 722−727.

(10) Derwand, R.; Scholz, M. Does zinc supplementation enhance the clinical efficacy of chloroquine/hydroxychloroquine to win today's battle against COVID-19? *Med. Hypotheses* **2020**, *142*, 109815.

(11) Carlucci, P. M.; Ahuja, T.; Petrilli, C.; Rajagopalan, H.; Jones, S.; Rahimian, J. Zinc Sulfate in Combination with a Zinc Ionophore May Improve Outcomes in Hospitalized COVID-19 Patients. *J. Med. Microbiol.* **2020**, *69*, 1228−1234.

(12) Wu, R.; Wang, L.; Kuo, H.-C. D.; Shannar, A.; Peter, R.; Chou, P. J.; Li, S.; Hudlikar, R.; Liu, X.; Liu, Z.; Poiani, G. J.; Amorosa, L.; Brunetti, L.; Kong, A.-N. An Update on Current Therapeutic Drugs Treating COVID-19. *Curr. Pharmacol. Rep.* **2020**, *6*, 56−70.

(13) te Velthuis, A. J. W.; van den Worm, S. H. E.; Sims, A. C.; Baric, R. S.; Snijder, E. J.; van Hemert, M. J. Zn2+ Inhibits Coronavirus and Arterivirus RNA Polymerase Activity In Vitro and Zinc Ionophores Block the Replication of These Viruses in Cell Culture. *PLoS Pathog.* **2010**, *6*, No. e1001176.

(14) Wessels, I.; Fischer, H. J.; Rink, L. Dietary and Physiological Effects of Zinc on the Immune System. *Annu. Rev. Nutr.* **2021**, *41*, 133−175.

(15) U.S. Government Information and Services. Indeed, the U.S. Food and Drug Administration (FDA) has revoked the authorization for emergency use of CQ and hydroxychloroquine and the NIH has recommended against their use for COVID-19 except in clinical trials. https://www.covid19treatmentguidelines.nih.gov/therapies/antiviral-therapy/chloroquine-or-hydroxychloroquine-and-or-azithromycin/ (accessed June 15, 2022).

(16) Xue, J.; Moyer, A.; Peng, B.; Wu, J.; Hannafon, B. N.; Ding, W.-Q. Chloroquine Is a Zinc Ionophore. *PLoS One* **2014**, *9*, No. e109180.

(17) Kavanagh, O. N.; Bhattacharya, S.; Marchetti, L.; Elmes, R.; O'Sullivan, F.; Farragher, J. P.; Robinson, S.; Thompson, D.; Walker, G. M. Hydroxychloroquine Does Not Function as a Direct Zinc Ionophore. *Pharmaceutics* **2022**, *14*, 899.

(18) Helm, L.; Merbach, A. E. Water Exchange on Metal Ions: Experiments and Simulations. *Coord. Chem. Rev.* **1999**, *187*, 151−181.

(19) Navarro, M.; Goitia, H.; Silva, P.; Velásquez, M.; Ojeda, L. E.; Fraile, G. Synthesis and characterization of new copper- and zinc-chloroquine complexes and their activities on respiratory burst of polymorphonuclear leukocytes. *J. Inorg. Biochem.* **2005**, *99*, 1630−1636.

(20) Navarro, M.; Hernández, C.; Vásquez, F.; Goitia, H.; Ojeda, L. E.; Velásquez, M.; Fraile, G. Syntheses, Characterization, and Biological Evaluation of New Zinc-and Gold-Chloroquine Diphosphate Complexes. *Transition Met. Chem.* **2008**, *33*, 893−898.

(21) Sánchez-Delgado, R. A.; Navarro, M.; Pérez, H.; Urbina, J. A. Toward a Novel Metal-Based Chemotherapy against Tropical Diseases. 2. Synthesis and Antimalarial Activity in Vitro and in Vivo of New Ruthenium− and Rhodium−Chloroquine Complexes. *J. Med. Chem.* **1996**, *39*, 1095−1099.

(22) Rosenberg, L. S.; Schulman, S. G. Tautomerism of Singly Protonated Chloroquine and Quinacrine. *J. Pharm. Sci.* **1978**, *67*, 1770−1772.

(23) Kavčič, H.; Umek, N.; Vintar, N.; Mavri, J. Local Anesthetics Transfer Relies on PH Differences and Affinities toward Lipophilic Compartments. *J. Phys. Org. Chem.* **2021**, *34*, No. e4275.

(24) Bray, P. G.; Janneh, O.; Raynes, K. J.; Mungthin, M.; Ginsburg, H.; Ward, S. A. Cellular Uptake of Chloroquine Is Dependent on Binding to Ferriprotoporphyrin IX and Is Independent of NHE Activity in Plasmodium Falciparum. *J. Cell Biol.* **1999**, *145*, 363−376.

(25) Banci, L.; Bertini, I.; Luchinat, C.; Scozzafava, A. Nuclear Relaxation in the Magnetic Coupled System Cu2Co2SOD. Histidine-44 Is Detached upon Anion Binding. *J. Am. Chem. Soc.* **1987**, *109*, 2328−2334.

(26) Arnesano, F.; Banci, L.; Piccioli, M. NMR Structures of Paramagnetic Metalloproteins. *Q. Rev. Biophys.* **2005**, *38*, 167−219.

(27) Egan, T. J. Interactions of Quinoline Antimalarials with Hematin in Solution. *J. Inorg. Biochem.* **2006**, *100*, 916−926.

(28) Wang, W.; Zhang, X.; Huang, D.; Zhu, H.; Chen, C.; Liu, Q. Quinolinium Trichloro(Quinoline)Zinc(II). *Acta Crystallogr., Sect. E: Struct. Rep. Online* **2001**, *57*, m561−m563.

(29) Toscano, P. J.; DiMauro, P. T.; Geremia, S.; Randaccio, L.; Zangrando, E. The Synthesis and Crystal Structure of [Cr(Acacen)-Py2] [ZnCl3py]. *Inorg. Chim. Acta* **1994**, *217*, 195−199.

(30) The aliphatic side chain at the exocyclic nitrogen was substituted by a methyl group for computational convenience (Figure 5).

(31) Liakos, D. G.; Neese, F. Improved Correlation Energy Extrapolation Schemes Based on Local Pair Natural Orbital Methods. *J. Phys. Chem. A* **2012**, *116*, 4801−4816.

(32) Riplinger, C.; Pinski, P.; Becker, U.; Valeev, E. F.; Neese, F. Sparse maps-A systematic infrastructure for reduced-scaling electronic structure methods. II. Linear scaling domain based pair natural orbital coupled cluster theory. *J. Chem. Phys.* **2016**, *144*, 024109.

(33) Guo, Y.; Riplinger, C.; Becker, U.; Liakos, D. G.; Minenkov, Y.; Cavallo, L.; Neese, F. Communication: An Improved Linear Scaling Perturbative Triples Correction for the Domain Based Local Pair-Natural Orbital Based Singles and Doubles Coupled Cluster Method [DLPNO-CCSD(T)]. *J. Chem. Phys.* **2018**, *148*, 011101.

(34) Becke, A. D. Density-functional thermochemistry. III. The role of exact exchange. *J. Chem. Phys.* **1993**, *98*, 5648−5652.

(35) Stephens, P. J.; Devlin, F. J.; Chabalowski, C. F.; Frisch, M. J. Ab Initio Calculation of Vibrational Absorption and Circular Dichroism Spectra Using Density Functional Force Fields. *J. Phys. Chem.* **1994**, *98*, 11623−11627.

(36) Weigend, F.; Ahlrichs, R. Balanced Basis Sets of Split Valence, Triple Zeta Valence and Quadruple Zeta Valence Quality for H to Rn: Design and Assessment of Accuracy. *Phys. Chem. Chem. Phys.* **2005**, *7*, 3297.

(37) These calculations favor a penta-coordination over a tetra-coordination in the gas phase (Section S5 in Supporting Information).

(38) Amin, E. A.; Truhlar, D. G. Zn Coordination Chemistry: Development of Benchmark Suites for Geometries, Dipole Moments, and Bond Dissociation Energies and Their Use To Test and Validate Density Functionals and Molecular Orbital Theory. *J. Chem. Theory Comput.* **2008**, *4*, 75−85.

(39) Weaver, M. N.; Merz, K. M.; Ma, D.; Kim, H. J.; Gagliardi, L. Calculation of Heats of Formation for Zn Complexes: Comparison of Density Functional Theory, Second Order Perturbation Theory, Coupled-Cluster and Complete Active Space Methods. *J. Chem. Theory Comput.* **2013**, *9*, 5277−5285.

(40) Hoops, S. C.; Anderson, K. W.; Merz, K. M. Force Field Design for Metalloproteins. *J. Am. Chem. Soc.* **1991**, *113*, 8262−8270.

(41) Peters, M. B.; Yang, Y.; Wang, B.; Füsti-Molnár, L.; Weaver, M. N.; Merz, K. M. Structural Survey of Zinc-Containing Proteins and Development of the Zinc AMBER Force Field (ZAFF). *J. Chem. Theory Comput.* **2010**, *6*, 2935−2947.

(42) Yu, Z.; Li, P.; Merz, K. M. Extended Zinc AMBER Force Field (EZAFF). *J. Chem. Theory Comput.* **2018**, *14*, 242−254.

(43) Genna, V.; Carloni, P.; De Vivo, M. A Strategically Located Arg/Lys Residue Promotes Correct Base Paring during Nucleic Acid Biosynthesis in Polymerases. *J. Am. Chem. Soc.* **2018**, *140*, 3312−3321.

(44) Genna, V.; Gaspari, R.; Dal PeraroDal Peraro, M.; De Vivo, M. Cooperative motion of a key positively charged residue and metal ions for DNA replication catalyzed by human DNA Polymerase-η. *Nucleic Acids Res.* **2016**, *44*, 2827−2836.

(45) Marzari, N.; Vanderbilt, D. Maximally Localized Generalized Wannier Functions for Composite Energy Bands. *Phys. Rev. B: Condens. Matter Mater. Phys.* **1997**, *56*, 12847−12865.

(46) Pearson, R. G. Hard and Soft Acids and Bases. *J. Am. Chem. Soc.* **1963**, *85*, 3533−3539.

(47) The zinc coordination bond lengths are overestimated as in the AIMD-BLYP simulation of CL2 (Table S4).

(48) Fatmi, M. Q.; Hofer, T. S.; Randolf, B. R.; Rode, B. M. Stability of Different Zinc(II)−Diamine Complexes in Aqueous Solution with

Respect to Structure and Dynamics: A QM/MM MD Study. *J. Phys. Chem. B* **2007**, *111*, 151−158.

(49) Kleifeld, O.; Frenkel, A.; Martin, J. M. L.; Sagi, I. Active Site Electronic Structure and Dynamics during Metalloenzyme Catalysis. *Nat. Struct. Biol.* **2003**, *10*, 98−103.

(50) Maret, W.; Li, Y. Coordination Dynamics of Zinc in Proteins. *Chem. Rev.* **2009**, *109*, 4682−4707.

(51) Another difference is due to the fact that MD covers a much shorter time scale (sub ns) than NMR (larger than ns). This might affect the residences time of water interacting with the ligand. These anyway are not the focus of the present paper.

(52) Zhao, Y.; Truhlar, D. G. A New Local Density Functional for Main-Group Thermochemistry, Transition Metal Bonding, Thermochemical Kinetics, and Noncovalent Interactions. *J. Chem. Phys.* **2006**, *125*, 194101.

(53) Stoychev, G. L.; Auer, A. A.; Izsák, R.; Neese, F. Self-Consistent Field Calculation of Nuclear Magnetic Resonance Chemical Shielding Constants Using Gauge-Including Atomic Orbitals and Approximate Two-Electron Integrals. *J. Chem. Theory Comput.* **2018**, *14*, 619−637.

(54) The H1' and C1' shifts are not compared here with experiment, because in the calculations a methyl group replaces the aliphatic part of CQ, adjacent to these atoms, profoundly modifying the chemical environment.

(55) Krężel, A.; Maret, W. The Biological Inorganic Chemistry of Zinc Ions. *Arch. Biochem. Biophys.* **2016**, *611*, 3−19.

(56) Rampal, N.; Wang, H.-W.; Biriukov, D.; Brady, A. B.; Neuefeind, J. C.; Předota, M.; Stack, A. G. Local Molecular Environment Drives Speciation and Reactivity of Ion Complexes in Concentrated Salt Solution. *J. Mol. Liq.* **2021**, *340*, 116898.

(57) Farrell, D.; Miranda, E. S.; Webb, H.; Georgi, N.; Crowley, P. B.; McIntosh, L. P.; Nielsen, J. E. Titration_DB: Storage and Analysis of NMR-Monitored Protein PH Titration Curves. *Proteins: Struct., Funct., Bioinf.* **2010**, *78*, 843−857.

(58) Schuth, N.; Mebs, S.; Huwald, D.; Wrzolek, P.; Schwalbe, M.; Hemschemeier, A.; Haumann, M. Effective intermediate-spin iron in O 2 -transporting heme proteins. *Proc. Natl. Acad. Sci.* **2017**, *114*, 8556−8561.

(59) Müller, O.; Nachtegaal, M.; Just, J.; Lützenkirchen-Hecht, D.; Frahm, R. Quick-EXAFS setup at the SuperXAS beamline forin situX-ray absorption spectroscopy with 10 ms time resolution. *J. Synchrotron Radiat.* **2016**, *23*, 260−266.

(60) Petuker, A.; Mebs, S.; Schuth, N.; Gerschel, P.; Reback, M. L.; Mallick, B.; van Gastel, M.; Haumann, M.; Apfel, U.-P. Spontaneous Si-C bond cleavage in (TriphosSi)-nickel complexes. *Dalton Trans.* **2017**, *46*, 907−917.

(61) Ankudinov, A. L.; Ravel, B.; Rehr, J. J.; Conradson, S. D. Real-Space Multiple-Scattering Calculation and Interpretation of x-Ray-Absorption near-Edge Structure. *Phys. Rev. B: Condens. Matter Mater. Phys.* **1998**, *58*, 7565−7576.

(62) Mukerji, I.; Andrews, J. C.; DeRose, V. J.; Latimer, M. J.; Yachandra, V. K.; Sauer, K.; Klein, M. P. Orientation of the Oxygen-Evolving Manganese Complex in a Photosystem II Membrane Preparation: An X-Ray Absorption Spectroscopy Study. *Biochemistry* **1994**, *33*, 9712−9721.

(63) Dau, H.; Liebisch, P.; Haumann, M. X-Ray Absorption Spectroscopy to Analyze Nuclear Geometry and Electronic Structure of Biological Metal Centers?Potential and Questions Examined with Special Focus on the Tetra-Nuclear Manganese Complex of Oxygenic Photosynthesis. *Anal. Bioanal. Chem.* **2003**, *376*, 562−583.

(64) Van Der Spoel, D.; Lindahl, E.; Hess, B.; Groenhof, G.; Mark, A. E.; Berendsen, H. J. C. GROMACS: Fast, Flexible, and Free. *J. Comput. Chem.* **2005**, *26*, 1701−1718.

(65) Lin, I.-C.; Seitsonen, A. P.; Tavernelli, I.; Rothlisberger, U. Structure and Dynamics of Liquid Water from ab Initio Molecular Dynamics-Comparison of BLYP, PBE, and revPBE Density Functionals with and without van der Waals Corrections. *J. Chem. Theory Comput.* **2012**, *8*, 3902−3910.

(66) Gillan, M. J.; Alfè, D.; Michaelides, A. Perspective: How Good Is DFT for Water? *J. Chem. Phys.* **2016**, *144*, 130901 American Institute of Physics Inc. April 7.

(67) Marx, D.; Hutter, J.*Ab Initio Molecular Dynamics*; Cambridge University Press, 2009.

(68) Troullier, N.; Martins, J. L. Efficient Pseudopotentials for Plane-Wave Calculations. *Phys. Rev. B: Condens. Matter Mater. Phys.* **1991**, *43*, 1993−2006.

(69) Berendsen, H. J. C.; Postma, J. P. M.; van Gunsteren, W. F.; DiNola, A.; Haak, J. R. Molecular Dynamics with Coupling to an External Bath. *J. Chem. Phys.* **1984**, *81*, 3684−3690.

(70) Nosé, S. A Unified Formulation of the Constant Temperature Molecular Dynamics Methods. *J. Chem. Phys.* **1984**, *81*, 511−519.

(71) Hoover, W. G. Canonical Dynamics: Equilibrium Phase-Space Distributions. *Phys Rev A (Coll Park)* **1985**, *31*, 1695−1697.

(72) Liberatore, E.; Meli, R.; Rothlisberger, U. A Versatile Multiple Time Step Scheme for Efficient Ab Initio Molecular Dynamics Simulations. *J. Chem. Theory Comput.* **2018**, *14*, 2834−2842.

(73) *CPMD* version 4.3, http://www.cpmd.org/; IBM Corp, 1990−2019, Copyright MPI für Festkörperforschung Stuttgart 1997−2001.

(74) Neese, F. The ORCA Program System. *WIREs Computational Molecular Science* **2012**, *2*, 73−78.

(75) Jensen, F. Segmented Contracted Basis Sets Optimized for Nuclear Magnetic Shielding. *J. Chem. Theory Comput.* **2015**, *11*, 132−138.

(76) Vahtras, O.; Almlöf, J.; Feyereisen, M. W. Integral Approximations for LCAO-SCF Calculations. *Chem. Phys. Lett.* **1993**, *213*, 514−518.

(77) Weigend, F. Hartree-Fock exchange fitting basis sets for H to Rn. *J. Comput. Chem.* **2008**, *29*, 167−175.

(78) Neese, F.; Wennmohs, F.; Hansen, A.; Becker, U. Efficient, approximate and parallel Hartree-Fock and hybrid DFT calculations. A "chain-of-spheres" algorithm for the Hartree-Fock exchange. *Chem. Phys.* **2009**, *356*, 98−109.

(79) Barone, V.; Cossi, M. Quantum Calculation of Molecular Energies and Energy Gradients in Solution by a Conductor Solvent Model. *J. Phys. Chem. A* **1998**, *102*, 1995−2001.

(80) Rehr, J. J.; Mustre de Leon, J.; Zabinsky, S. I.; Albers, R. C. Theoretical X-Ray Absorption Fine Structure Standards. *J. Am. Chem. Soc.* **1991**, *113*, 5135−5140.

(81) Rehr, J. J.; Albers, R. C.; Zabinsky, S. I. High-Order Multiple-Scattering Calculations of x-Ray-Absorption Fine Structure. *Phys. Rev. Lett.* **1992**, *69*, 3397−3400.

(82) Rehr, J. J.; Albers, R. C. Theoretical Approaches to X-Ray Absorption Fine Structure. *Rev. Mod. Phys.* **2000**, *72*, 621−654.

(83) Newville, M. Larch: An Analysis Package for XAFS and Related Spectroscopies. *J. Phys.: Conf. Ser.* **2013**, *430*, 012007.